

1 **Seasonal variability in warm-water inflow towards Kangerdlugssuaq Fjord**

2 Renske Gelderloos*

3 *Department of Earth and Planetary Sciences, Johns Hopkins University, Baltimore, Maryland*

4 Thomas W. N. Haine

5 *Department of Earth and Planetary Sciences, Johns Hopkins University, Baltimore, Maryland*

6 Inga M. Koszalka

7 *GEOMAR-Helmholtz Centre for Ocean Research, Kiel, Germany*

8 Marcello G. Magaldi

9 *Istituto di Scienze Marine, S.S. di Lerici, Consiglio Nazionale delle Ricerche, Lerici, Italy, and*

10 *Department of Earth and Planetary Sciences, The Johns Hopkins University, Baltimore,*

11 *Maryland*

12 *Corresponding author address: Department of Earth and Planetary Sciences, Johns Hopkins Uni-
13 versity, 328 Olin Hall, 3400 North Charles Street, Baltimore, MD 21218

14 E-mail: rgelder2@jhu.edu

ABSTRACT

15 Seasonal variability in pathways of warm water masses toward the Kangerd-
16 lugssuaq Fjord-Glacier system (KF/KG), southeast Greenland, is investigated
17 by backtracking Lagrangian particles seeded at the fjord mouth in a high-
18 resolution regional ocean model simulation in the ice-free and the ice-covered
19 seasons. The waters at KF are a mixture of Atlantic-origin water advected
20 from the Irminger Basin (FF for Faxaflói), the deep waters from the Denmark
21 Strait and the waters from the Arctic Ocean, both represented by the Kögur
22 section (KO). Below 200m depth, the warm water is a mixture of FF and KO
23 water masses, and is warmer in winter than in summer. We find that seasonal
24 differences in pathways double the fraction of FF particles in winter, caus-
25 ing the seasonal warming and salinification. Seasonal temperature variations
26 at the upstream sections (FF and KO) have a negligible impact on tempera-
27 ture variations near the fjord. Successful monitoring of heat flux to the fjord
28 therefore needs to take place close to the fjord, and cannot be inferred from
29 upstream conditions.

30 **1. Introduction**

31 The Greenland Ice Sheet (GIS) has been losing mass at an accelerating rate over the past two
32 decades (IPCC 2013; Shepherd et al. 2012; Velicogna and Wahr 2013; Groh et al. 2014; Khan
33 et al. 2015). A quadrupling of the loss over this period has increased its current sea-level rise
34 contribution to 25 % of the total (Straneo and Heimbach 2013; Straneo and Cenedese 2015), with
35 a significant sea-level fingerprint in remote locations (Brunnabend et al. 2015; Rietbroek et al.
36 2016). GIS melt water impacts the local ocean circulation and may in the future also affect the
37 global ocean circulation through its impact on the Labrador Sea surface salinity, convection, and
38 thereby the Atlantic Meridional Overturning Circulation (Rahmstorf et al. 2015; Boning et al.
39 2016).

40 The striking simultaneous retreat of the Greenland glaciers has pointed towards environmental
41 causes rather than (only) internal glacier dynamics (Luckman et al. 2006; Murray et al. 2010; Seale
42 et al. 2011; Straneo et al. 2013). Next to atmospheric warming due to climate change, intrusion
43 of warm water masses into the Greenland fjords and a possible connection to the changes in the
44 heat content in the lower latitudes have been proposed as an important factor (Holland et al. 2008;
45 Christoffersen et al. 2012; Straneo and Heimbach 2013). The consequences of warm ocean water
46 intrusion include undercutting of the glacial front (Hanna et al. 2009; Thomas et al. 2009) and
47 a reduction of the sea ice cover, which in turn leads to higher atmospheric temperatures through
48 a lowered albedo and potentially destabilization of ice melange on the calving front (Seale et al.
49 2011).

50 About half of the increased GIS mass loss is attributed to acceleration of the southeastern and
51 western outlet glaciers (van den Broeke et al. 2009; Rignot et al. 2010; Straneo et al. 2013;
52 Velicogna and Wahr 2013), of which Kangerdlugssuaq Glacier (KG) is the third largest contributor

53 (Enderlin et al. 2014). KG underwent a major thinning of more than 100 m after 2003, and the
54 records of glacier front positions and elevation suggest a complicated behavior that is not always
55 captured by ice-sheet models (Khan et al. 2014). The interaction between glaciers and the adjacent
56 ocean is complicated, however, and depends on local and poorly-understood factors such as fjord
57 dynamics and buoyant plumes at the glacier-ocean interface (Straneo and Cenedese 2015).

58 Some key unknowns include the pathways of warm waters to the glacial fjords and the attendant
59 hydrographic variability. Located just south of Denmark Strait, KF is positioned at a confluence
60 of ocean currents (Figure 1): On the shelf, the East Greenland Current (EGC) carries cold and
61 fresh water from the Arctic (Rudels et al. 2002; Sutherland and Pickart 2008). At the shelf break,
62 the warm and saline Irminger Current carries water of subtropical North Atlantic origin which is
63 slightly denser than the fresh water on the shelf (e.g. Rudels et al. 2002). At greater depth dense
64 waters are found, formed by intense mixing of cascading Denmark Strait Overflow Water (DSOW)
65 with the surrounding water masses (Price and Baringer 1994; Koszalka et al. 2013) and continuing
66 onwards in the deep western boundary current.

67 Although the general pattern of the regional ocean circulation in this area is well established
68 (e.g. Rudels et al. 2002), very little is known about the interaction between the deep ocean and the
69 shelf and seasonal variability therein. The confluence of ocean currents, combined with sea ice
70 and a complicated bathymetry, make this a difficult area to observe. A compilation of 2004-2010
71 summertime seal-borne temperature data (Sutherland et al. 2013) showed that the cold EGC water
72 is clearly visible above 150 m depth on the shelf. Atlantic-origin water is generally located sea-
73 wards of the shelf, but upstream of Kangerdlugssuaq Trough it appears on the shelf. In addition
74 to the summertime survey, the seasonal variability near Sermilik Fjord (downstream of Kangerd-
75 lugssuaq; Figure 1) was also studied in that paper: While the deeper waters were warm year-round,
76 in some locations the water shallower than 200 m was warm in summer and fall, and cold in winter

77 and spring. Because this seasonality was location dependent, Sutherland et al. (2013) hypothesized
78 that variations in Irminger-Current pathways could be responsible.

79 *In situ* observations inside Kangerdlugssuaq Fjord are limited to a few synoptic summertime
80 surveys (Azetsu-Scott and Tan 1997; Christoffersen et al. 2012; Sutherland et al. 2014; Inall et al.
81 2014) and one wintertime mooring (Jackson et al. 2014). These observations have confirmed the
82 presence of warm water in the fjord, but some important questions remain: Where did this warm
83 water come from, where and how did it cross the continental shelf, where did the water obtain
84 its heat, and is there any seasonal variability in the heat delivery, and, as a consequence, how
85 representative are summertime observations for annual-mean conditions?

86 The aim of this study is to address these questions. We address them using a year-long simulation
87 of a very high-resolution regional model in combination with a Lagrangian particle-tracking tool.
88 Based on *in situ* observations and knowledge of the regional circulation (Figure 1), three potential
89 sources of warm water have been identified: (1) warm Polar Surface Water (PSWw) is carried
90 by the fresh EGC and has gained heat from interaction with the solar-warmed top layer on its
91 way south; (2) warm and saline Atlantic Water (AW) is brought in by the Irminger Current at
92 intermediate depths, and (3) DSOW is the dense water found at the bottom of the fjord, underneath
93 the AW. By tracing the origin of the water that enters Kangerdlugssuaq Fjord in our model, we can
94 form a kinematic picture of the time-varying water pathways. The focus of this manuscript is on
95 identifying these pathways and on the impacts of changing pathways on the warm water delivery
96 to the fjord entrance; the mechanisms that would cause these pathways to be different, which could
97 include the presence of sea ice, different local as well as remote wind conditions, thermohaline
98 forcing at the surface and internal ocean dynamics, are beyond the scope of the present study.
99 Throughout the manuscript, we will refer to differences between the summer and winter of the

100 2007/2008 year as seasonal variability. As the seasonal cycle is much larger than interannual
101 trends, other years may show quantitatively, but probably not qualitatively, different results.

102 A description of the ocean model setup and the Lagrangian particle-tracking algorithm are given
103 in Section 2. This section also covers model validation, a description of seasonal variability in the
104 model, and a description of the setup of the particle-tracking simulations. Section 3 explores the
105 particle pathways to the fjord and their seasonal dependence. In Section 4 along-path water mass
106 transformation is investigated. The results are summarized in Section 5.

107 **2. Methods**

108 *a. Ocean circulation and sea ice model*

109 For a detailed representation of the circulation in this area, a regional ocean and sea ice model of
110 the Irminger Sea and adjacent Greenland Shelf (Figure 1) was created using the MITgcm (Marshall
111 et al. 1997). The configuration builds upon previous setups (Magaldi et al. 2011; Koszalka et al.
112 2013; von Appen et al. 2014), which realistically captured the surface circulation, dense water
113 transport, and the structure and transport through characteristic synoptic sections. To study the
114 circulation in the vicinity of KF, several improvements were implemented as described below.

115 The nominal horizontal resolution is 2 km, and the layer thickness varies from 2 m near the
116 surface to 15 m below 110 m depth. The model was run in hydrostatic mode for the period
117 1 June 2007 to 31 May 2008, after an initial 17-month spinup as described in Magaldi et al.
118 (2011). During the simulation, sea surface temperatures were relaxed on a 5-day time scale to the
119 Operational Sea Surface Temperature and Sea Ice Analysis (OSTIA) product (Donlon et al. 2012).
120 Surface forcings are based on ERA-Interim reanalysis fields (Dee et al. 2011). This product has
121 been previously shown to adequately represent the scale and strength of winds in the region of

122 interest (Harden et al. 2011), and to resolve high-frequency, down-slope wind events that influence
123 the sea ice conditions in southeast Greenland fjords (Oltmanns et al. 2014). A further improvement
124 is the inclusion of ship- and seal-borne measurements of bathymetry (Sutherland et al. 2013),
125 which improves the representation of the shelf circulation.

126 At the three open boundaries, velocities and tracer values are prescribed from a global HYCOM
127 simulation (Chassignet et al. 2009), while Greenland forms a naturally closed boundary at the west
128 side of the domain. A no-slip boundary condition is used for both bottom and side walls. The KPP
129 scheme with a background vertical viscosity of $10^{-5} \text{ m}^2 \text{ s}^{-1}$ is used (Large et al. 1994) and the
130 Leith scheme for horizontal viscosity is applied (Leith 1967).

131 The ocean model is coupled to a viscous-plastic dynamic/thermodynamic sea ice model, as
132 described in Menemenlis et al. (2005), Losch et al. (2010) and Heimbach et al. (2010). Sea ice and
133 snow thicknesses, sea ice fraction and salinity are all advected by ice velocities via a second-order
134 scheme with flux limiters. Salt rejected during sea ice formation is treated using the subgrid-scale
135 salt plume parameterization of Nguyen et al. (2009). Open boundary conditions for all sea-ice
136 variables are obtained from the $1/8^\circ$ TOPAZv4 (Towards an Operational Prediction system for the
137 north Atlantic european coastal Zone, version 4) monthly reanalysis data (Sakov et al. 2012). The
138 interior sea-ice fields are nudged to the TOPAZ reanalysis values within 20 points of the grid edge.
139 The nudging time scale is 1 day at the boundaries and linearly increases toward the interior to reach
140 the maximum value of 10 days. There is no spinup for sea ice; the initial sea-ice conditions are
141 derived from the TOPAZv4 reanalysis data for May 2007.

142 *b. Mean hydrographic properties at the control sections*

143 The general ocean circulation, volume fluxes and water properties in the ocean model have
144 been compared to observations at the standard sections along the boundary current system in the

145 Irminger Basin with a very good agreement (Denmark Strait, Spill Jet, Angmagssalik; see Magaldi
146 et al. 2011; Koszalka et al. 2013), and we therefore focus here on the hydrographic properties at
147 the control sections used in this study. Particle trajectories are traced back from the KF entrance
148 to two upstream control sections, chosen to coincide with known hydrographic repeat sections
149 (Figure 1): Between Iceland and Greenland, just upstream of Denmark Strait, the Kögur section
150 (KO) captures water masses flowing in from the Arctic and Nordic Seas. The Faxaflói section
151 (FF) west of Iceland captures the warm and saline water of subtropical origin in the Irminger
152 current. All available high resolution CTD (Conductivity, Temperature, and Depth) observations
153 in this area were extracted from the World Ocean Database (Boyer et al. 2013), and all stations
154 within 5 km of the respective hydrographic sections were mapped onto the sections and compared
155 to the annual-mean hydrography from the model (Figures 2 and 3). The FF composite contains
156 440 stations taken between 1996 and 2011; the KO composite is comprised of 314 stations taken
157 between 1982 and 2011.

158 The FF comparison in Figure 2 shows excellent agreement in the potential temperature structure
159 (panels a and c), and a slightly less saline top 500 m in the model compared to observations (panels
160 b and d). The difference is small and likely due to the fact that most observations were taken in
161 summer, when the stratification is stronger. The KO comparison in Figure 3 shows again excellent
162 agreement for potential temperature (panels a and c), with a small difference in structure on the
163 Iceland side (right-hand side in the figure) of the section. The KO salinity comparison (panels b
164 and d) shows that the model is biased salty in the top 100 m. One might expect that this is in fact
165 a bias in the (mostly summertime) observations, as sea-ice melt reduces the near-surface salinity.
166 However, the model summer-mean is also too salty (Figure 3f), and we have verified that this bias
167 is inherited from a too salty EGC in the boundary conditions. The subsurface, however, shows
168 very good agreement.

169 The upstream control sections, which can be directly compared with observations, thus show
170 realistic θ/S properties. The particle-release section (Kangerdlugssuaq Section, KS, cyan line in
171 Figure 1) was chosen outside of the fjord, because the model resolution is not sufficiently high
172 to capture the details of the fjord circulation. Observations at this section are not available, but
173 the World Ocean Database does contain CTD observations on a section just north of KS from
174 September 2007, which we will refer to as KS' (magenta line in Figure 1) and use for comparison
175 with model data on this same section. Because of the limited amount of data, comparison is not
176 performed on the annual mean but on the late September fields.

177 Figure 4 shows the potential temperature (top panels), salinity (middle panels), and potential
178 density (bottom panels) from observations on 28 September 2007 (right) and its model equiva-
179 lent averaged from 5 days before to 5 days after this date to eliminate short-term variability (left).
180 In the bottom panels, the water masses according to Inall et al. (2014) are overlaid in colored
181 dashed contour lines. The water mass comparison shows that the Denmark Strait Overflow Water
182 (DSOW), modified Atlantic Water (AWm), and warm Polar Surface Water (PSWw) are all present
183 and found in the same depth ranges. The cold layer of Polar Surface Water (PSW) is somewhat
184 deeper in the model than in observations. Furthermore, as glacial melt and runoff were not in-
185 cluded in the model simulation, the very fresh surface water found in observations is absent in the
186 model fields. The somewhat lower model salinities in the upper 200 m are furthermore consis-
187 tent with the salinity bias found in the EGC at the Kögur section. The subsurface hydrographic
188 properties are in good agreement.

189 The above model validation confirmed that the model reproduces the mean hydrographic prop-
190 erties from observations well. In the remainder of this manuscript we will therefore focus on the
191 model output fields.

192 *c. Seasonal variability at the control sections*

193 The central question in this study concerns the differences in pathways between the summer
194 (ice-free) and the winter (ice-covered) seasons. We therefore split the model output in two five-
195 month periods: July-November (hereafter referred to as JASON), when the area around KF/KT is
196 ice free, and January-May (JFMAM), when the shelf region is covered in sea ice.

197 At the particle release site KS (Figure 5), the water below 200 m depth is warmer and saltier
198 in winter than in summer. The top 200 m, on the other hand, is colder and slightly fresher. As a
199 result, the water column in winter is more strongly stratified.

200 The seasonal fields at the upstream FF section (Figure 2e-h) show similar variability, though
201 much less pronounced in the subsurface: The top circa 500 m is about 1 °C warmer in the summer
202 season, but below this depth the water is slightly warmer in winter. The salinity in the lower water
203 column changes little over the year, but the upper 500 m is well mixed in winter, thereby reducing
204 the salinity on the Iceland shelf and increasing it on the slope and further offshore. In contrast to
205 KS, stratification is therefore weaker in winter at FF. Variability at the other upstream section (KO,
206 Figure 3e-h) is similar to that at FF. The top 500 m is warmer and more stratified in summer than
207 in winter. Below this depth the θ/S characteristics are very similar.

208 To study to what extent θ/S properties are inherited from upstream conditions, and how the path
209 taken to reach the fjord entrance affects changes in these characteristics, Lagrangian particles are
210 released at KS and traced back to either FF or KO. The remainder of this section discusses details
211 of the Lagrangian particle-tracking algorithm and the specific simulation setup choices used in this
212 study.

213 *d. Lagrangian particle tracking model*

214 The numerical particle trajectories are simulated offline using a particle tracking algorithm from
215 Koszalka et al. (2013); see also Gelderloos et al. (2016). The discrete MATLAB software employs
216 a trapezoidal solver with a 2nd-order predictor and 3rd-order corrector scheme. The particles
217 are advanced with the three-dimensional model velocity linearly interpolated on instantaneous
218 particle positions. For the boundary conditions, the velocity component normal to the bathymetric
219 boundary is zero, so that particles slide along the bottom and walls of the domain. There is no
220 explicit diffusion in the particle code. The tracer fields are linearly interpolated onto the particle
221 positions to obtain time series of salinity and temperature.

222 The particle-tracking algorithm uses 6-hourly snapshots from the ocean model as input. We
223 conducted a sensitivity study and found that a 6-hour time interval for the ocean model output is
224 sufficient to resolve the flow variability on the East Greenland shelf, and attain a convergence of
225 ensemble particle position and travel time statistics (Koszalka et al. 2017, manuscript in prepara-
226 tion).

227 *e. Setup of the simulations*

228 A total of 1274 particles are seeded twice a day at the KS section near the fjord entrance. They
229 are spaced 500 m in the horizontal and 25 m in the vertical, and occupy the 50-500 m depth range.
230 Particles are seeded in May and November (the last months of our winter and summer seasons)
231 with 61 releases in each month. The total number of particles tracked is thus about 155000.

232 The particles are tracked backwards in time for 5 months. A year-long sensitivity study with
233 3822 particles showed that over 80 % of the particles that reach either the KO or FF section (83 %
234 of the total) do so within this period. 15 % of the particles are killed because they come within 5 m
235 of the surface; less than 2 % remain in the subsurface, but do not reach either section within a year.

236 Important to note is that the statistics on θ/S transformation from KO/FF to KS do not change for
237 simulations of 4 months or longer. Only particles that could be traced back to either the KO or
238 the FF section are included in the analysis. The two sections represent distinct sources, as only a
239 negligible fraction ($\ll 1\%$) of KO particles originated in the Irminger Basin and FF particles in
240 the Nordic Seas.

241 **3. Preferred pathways**

242 *a. A horizontal view*

243 The pathways followed by particles approaching KF are visualized in Figure 6. The figure
244 shows the likelihood that an area will be visited by a particle in the given season. Although some
245 significant differences between the seasons are clear, parts of the pathways are common to both
246 seasons and notably influenced by bathymetry. In particular, the KT steers the flow towards the
247 fjord entrance.

248 The KO particles (blue shading) show the largest seasonal variability. A coastal route appears
249 in both summer and winter, but a second (offshore) pathway crosses onto the shelf around 67.5°N
250 in summer, while it follows the continental slope and takes the long way around Dohrn Bank and
251 into KT in winter. Given the fact that sea ice overlies the summertime crossing location onto the
252 shelf (Figure 6), the presence or absence of the sea ice could play a role in changing the preferred
253 route.

254 The FF particles (red shading) exhibit less variation with season. They generally follow the rim
255 of the Irminger Basin into Denmark Strait as previously described by Rudels et al. (2002), and then
256 return to the Irminger Basin and into the KT. A small fraction of the FF particles follows a route

257 northwards through Denmark Strait and then onto the shelf in summer, but like the KO particles,
258 in the winter months trajectories are restricted to the KT.

259 The seasonal difference in preferred routes leads to different typical transit times from the up-
260 stream control sections to KS (Figure 7). Both source waters take longer to reach the fjord in
261 winter than in summer: the median transit time for FF particles increases from 56 to 73 days,
262 while the median transit time for KO particles doubles from 44 to 97 days. In summer, the fastest
263 route is thus from the KO section, while in winter the FF particles reach the fjord first. This is
264 reflected in the fractionation between the two sources (Figure 8): In summer, 9 % of particles
265 originates from FF, while in winter this fraction doubles to 20 %.

266 *b. Vertical distribution in the water column*

267 The observations and model sections in Figure 4 showed that the different water masses typically
268 occupy a certain depth range at KS: PSWw at the top, AWm at middepth, and DSOW in the
269 deepest part of the water column. Figure 8 (solid lines) shows how many particles (as a fraction
270 of the total traced number in that season) from a certain control section arrive at a certain depth at
271 KS. It shows that the observed water mass distribution roughly corresponds to the water masses
272 from our upstream control sections: The FF-origin particles are mostly found in the 200-400 m
273 depth range, while the KO particles occupy the top 200 m and the lowest part of the water column.

274 While the qualitative pattern is similar in winter and summer, the stratification is much more
275 pronounced in winter. In summer, both the FF and KO particles are more spread out over the
276 water column, while in winter KO particles seem to avoid the central depth range. These findings
277 are in line with the increased stratification in winter at KS (Figure 5).

278 **4. Seasonal variations in θ/S transformation**

279 The significantly larger volume fraction of FF-origin particles in winter (Figure 8) could explain
280 the warmer and more saline subsurface at KS in that season (Figure 5). To confirm this hypothesis,
281 we now look at the θ/S properties of the water particles as a measure for the heat and salt they
282 carry to the fjord entrance.

283 *a. Particle- θ/S properties at the control sections*

284 Figure 9a/b shows the θ/S transformation of the particles from their upstream control sections
285 to the KS section at the fjord entrance in a θ/S diagram. The particles that travel from the FF
286 to the KS section (red to magenta) start out at roughly the same salinity in both seasons, but
287 summer particles have a 0.5 °C higher temperatures on average. They cool and freshen along
288 their trajectories in both seasons, but nearly 2 °C/0.25 psu more in summer. The particles that
289 travel from the KO to the KS section (blue to green) show a different behavior. In summer, their
290 average properties hardly change, i.e. the widespread cooling of the particles in the upper layers
291 in the latter months of this season is offset by mixing with the warmer water in the Irminger Basin.
292 Cooling in winter is much stronger, and therefore the mean temperature, dominated by the larger
293 number of particles in the upper part of the water column (Figure 8) goes down in this season. The
294 mean freshening occurs because the sea ice is starting to melt in the latter part of this period.

295 The water mass transformation of FF particles seems peculiar, as the particles are warmer at
296 the FF section in summer than in winter, but cool so much in summer that the average potential
297 temperature is lower by the time they reach the KS section than it is in winter. So, the faster
298 pathway from the FF section in winter appears to facilitate a doubling of the fraction of FF particles
299 in that season, causing the water to be warmer and more saline (Figure 9a/b).

300 *b. Localization of mixing*

301 A plausible cause of enhanced cooling and freshening of the FF particles in summer is increased
302 mixing with the colder and fresher water masses from the KO section. The pathways in Figure 6
303 suggest that the water masses come into contact with one another and are able to exchange prop-
304 erties. The Lagrangian framework uniquely enables spatial mapping of these property changes
305 along particle paths. The rate of change of temperature was extracted from the two particle sets,
306 spatially binned, and then averaged. Figure 10 shows in red shading the regions where FF particles
307 lose heat at a rate larger than 0.02 °C per day, and in blue the regions where KO particles gain heat
308 at a rate larger than 0.02 °C per day. The figure shows that the regions where KO particles gain
309 heat coincide with the regions where FF particles lose heat, in particular south of Denmark Strait
310 in the Dohrn Bank area, which is in line with previous work by Koszalka et al. (2013).

311 *c. Seasonal variability in mixing rates*

312 To quantify the amount of en-route mixing, we make two assumptions: First, below 200 m depth
313 (where the FF particles are found at KS) there are no other sources of heat and salt than water
314 coming through the KO and FF sections, i.e. the impact of ocean-atmosphere exchange on the
315 water properties at depth are minimal; second, the θ/S characteristics of the particles from KO/FF
316 are representative of the water mass properties of water going through these sections (compare
317 Figures 2e-h and 3e-h with Figure 9). With these assumptions, the water mass properties at KS are
318 a simple linear function of the upstream properties and mixing ratios, as calculated from mixing
319 the FF and KO water masses along a straight line in θ/S space (Gill 1982) using the volume ratios

320 based on the particle fractions:

$$\begin{bmatrix} \theta_{KS} \\ S_{KS} \end{bmatrix} = f_{V,FF} \begin{bmatrix} \theta_{FF} \\ S_{FF} \end{bmatrix} + f_{V,KO} \begin{bmatrix} \theta_{KO} \\ S_{KO} \end{bmatrix} \quad (1)$$

321 where f_V is the volume fraction of the water mass, according to

$$f_{V,FF}(z_k, \text{SEAS}) = \frac{f_{FF}(z_k, \text{SEAS})}{f_{FF}(z_k, \text{SEAS}) + f_{KO}(z_k, \text{SEAS})}$$

322 where $f_{FF}(z_k, \text{SEAS})$ are the fractions from Figure 8 for discrete release depth z_k and season
323 SEAS. θ and S the potential temperature and salinity at the control sections. All variables are a
324 function of release depth and season.

325 Instead of solving for S_{KS} and θ_{KS} , we use the values from the ocean model (Figure 5) and
326 solve for the required volume fractions to produce these hydrographic properties (dashed line with
327 triangles in Figure 8). As expected, the linear mixing model performs poorly in the upper 200 m,
328 especially in winter, where nearly all particles originate from the KO section and water properties
329 changes are determined largely by atmosphere-ocean and/or ice-ocean interaction. Below 200 m,
330 however, the mixing model predicts the ocean model θ/S properties very well.

331 Now that we have established that the linear mixing model is appropriate for the depth range at
332 KS that warms and salinifies in the winter season, we will use this model to determine whether the
333 seasonal variability is determined mostly by the seasonal variability of the θ/S properties of the
334 upstream control sections, or by seasonal variability in mixing of the water masses.

335 First, we make slight adjustments to the volume fractions so that the calculated θ/S properties
336 exactly match the ocean model values (above 200 m, the adjustment is large, but we include these
337 values for completeness). The θ/S properties thus found are plotted in Figure 9c/d as the black
338 squares. Second, we repeat the calculation, but instead of using seasonally varying values for the
339 water properties θ_{FF} , S_{FF} , θ_{KO} , and S_{KO} , we use their annual mean values. The hypothetical θ_{KS}

340 and S_{KS} calculated are plotted as the cyan asterisks in Figure 9c/d. In the top layers (cold/fresh
341 corner of the θ/S diagram), the models match poorly as expected. In the lower part of the water
342 column, however, there is a surprisingly good agreement. Third, the hydrographic properties are
343 allowed to vary with season, but the volume fractions are held constant at their annual mean value.
344 The resulting θ_{KS} and S_{KS} are the magenta symbols in Figure 9c/d. Clearly, not incorporating
345 seasonal variability in mixing rates yields large deviations from the model- θ/S properties at KS,
346 while ignoring seasonal variations in upstream θ/S properties has very little effect.

347 **5. Summary and discussion**

348 In this study the pathways and along-path transformation of warm water masses towards
349 Kangerdlugssuaq Fjord were investigated in a Lagrangian framework using a very high-resolution
350 model. Based on the water masses found near the fjord entrance, two sections were identified to
351 distinguish between different regions of origin. They are: The Kögur hydrographic repeat sec-
352 tion (KO) between Iceland and Greenland, accounting for contributions of waters from the Nordic
353 Seas, and the zonal Faxaflói hydrographic repeat section (FF) west of Iceland, covering water mass
354 contributions from the Irminger Basin. Neutrally-buoyant particles were seeded near the fjord en-
355 trance (KS section) and backtracked in the full 3-D velocity field for a period of five months to
356 identify the origin of the particles. Only particles that crossed at least one of the two sections of
357 origin were analyzed.

358 The analysis showed that in the top 200 m of the water column the water almost exclusively
359 originates from the KO section. FF particles are found between 200 and 400 m depth and form the
360 main water mass there in winter. In the lowest part of the water column, the KO section is again
361 the dominant source.

362 Both the pathways and properties of the water masses vary seasonally. In both seasons the FF
363 particle trajectories follow the bathymetry into Kangerdlugssuaq Trough, while some go north
364 through Denmark Strait and then across the shelf. In contrast to the results of Sutherland et al.
365 (2013) for the shelf region around Sermilik Fjord, we do not find that FF water occupies the whole
366 water column in summer, but rather the FF water mass is more spread out in summer, and actually
367 more dominant in the winter season. The differences between our results and those of Sutherland
368 et al. (2014) are likely due to differences in the data distribution, in particular the tendency of seals
369 to visit only certain regions (these more biologically productive), while the Lagrangian particles
370 trace the flow pathways. The KO particles follow a coastal route year-round and a more offshore
371 route that varies seasonally: it crosses the shelf in summer, but follows the bathymetry around
372 Dohrn Bank into Kangerdlugssuaq Trough in winter.

373 The seasonal differences in pathways is reflected in the particle travel times. In summer, the
374 KO particles are the first to arrive at the KS sections with a median travel time of 44 days vs 56
375 days for FF particles. The longer, offshore KO route in winter doubles the travel time to 97 days,
376 however, while FF particles only take 73 days, making the FF travel time the shortest in winter.
377 With the KO particles taking a longer route in winter, the fraction of FF particles at KS doubles
378 from 9 % in summer to 20 % in winter, causing a warmer and more saline water mass at KS in
379 winter below 200 m depth.

380 Although the water mass properties at the control sections show a pronounced seasonal variabil-
381 ity, the impact of these variations on the θ/S properties at KS is negligible compared to seasonal
382 variations in the mixing fractions. For this reason, we conclude that *in situ* monitoring of the heat
383 flux to Kangerdlugssuaq Fjord likely requires measurements close to the fjord, as seasonal varia-
384 tions in the upstream water mass properties are not inherited at the fjord entrance. Furthermore,
385 although we cannot make firm statements on interannual variability based on a 1-year simulation,

386 we conjecture that long-term changes in upstream hydrographic conditions that are small com-
387 pared to the seasonal cycle may be masked by variations in mixing rates. Possible indirect effects
388 through changes in the circulation have, however, not been investigated in this study. Finally, in-
389 terannual or decadal variations in the sea ice characteristics off East Greenland are likely important
390 for variations in the offshore KO route in winter, and thus likely impact interannual variability in
391 mixing rates.

392 *Acknowledgments.* This work was supported by NSF grants OCE-1433448 and OCE-1129895.

393 **References**

394 Azetsu-Scott, K., and F. C. Tan, 1997: Oxygen isotope studies from Iceland to an East Greenland
395 Fjord: behaviour of glacial meltwater plume. *Marine Chemistry*, **56**, 239–251.

396 Boning, C. W., E. Behrens, A. Biastoch, K. Getzlaff, and J. L. Bamber, 2016: Emerging impact of
397 Greenland meltwater on deepwater formation in the North Atlantic Ocean. *Nature Geoscience*,
398 **9**, 523527, doi:10.1038/ngeo2740.

399 Boyer, T. P., and Coauthors, 2013: World Ocean Database 2013, NOAA Atlas NES-
400 DIS 72, S. Levitus, Ed., A. Mishonov, Technical Ed.; Silver Spring, MD, 209 pp.,
401 <http://doi.org/10.7289/V5NZ85MT>.

402 Brunnabend, S.-E., J. Schrter, R. Rietbroek, and J. Kusche, 2015: Regional sea level change in
403 response to ice mass loss in Greenland, the West Antarctic and Alaska. *Journal of Geophysical*
404 *Research Oceans*, **120**, 7316–7328, doi:10.1002/2015JC011244.

405 Chassignet, E. P., and Coauthors, 2009: US GODAE: Global ocean prediction with the HYbrid Co-
406 ordinate Ocean Model (HYCOM). *Oceanography*, **22**, 64–75, URL [http://dx.doi.org/10.5670/](http://dx.doi.org/10.5670/oceanog.2009.39)
407 [oceanog.2009.39](http://dx.doi.org/10.5670/oceanog.2009.39).

- 408 Christoffersen, P., M. O’Leary, J. H. van Angelen, and M. van den Broeke, 2012: Partitioning
409 effect from ocean and atmosphere on the calving stability of Kangerdlugssuaq Glacier, East
410 Greenland. *Annals of Glaciology*, **53**, 249–256, doi:10.3189/2012AoG60A087.
- 411 Dee, D. P., and Coauthors, 2011: The ERA-Interim reanalysis: configuration and performance
412 of the data assimilation system. *Quarterly Journal of the Royal Meteorological Society*, **137**,
413 553–597, doi:10.1002/qj.828.
- 414 Donlon, C. J., M. Martin, J. D. Stark, J. Roberts-Jones, E. Fiedler, and W. Wimmer, 2012: The
415 Operational Sea Surface Temperature and Sea Ice Analysis (OSTIA). *Remote Sensing of Envi-
416 ronment*, **116**, 140–158, doi:10.1016/j.rse.2010.10.017.
- 417 Enderlin, E. M., I. M. Howat, S. Jeong, M.-J. Noh, J. H. van Angelen, and M. R. van den Broeke,
418 2014: An improved mass budget for the Greenland ice sheet. *Geophysical Research Letters*, **41**,
419 866–872, doi:10.1002/2013GL059010.
- 420 Gelderloos, R., A. S. Szalay, T. W. N. Haine, and G. Lemson, 2016: A fast algorithm for neutrally-
421 buoyant lagrangian particles in numerical ocean modeling. *12th IEEE International Conference
422 on e-Science, e-Science 2016, Baltimore, MD, USA, October 23-27, 2016*, 381–388, doi:10.
423 1109/eScience.2016.7870923, URL <http://dx.doi.org/10.1109/eScience.2016.7870923>.
- 424 Gill, A. E., 1982: *Atmosphere-Ocean Dynamics*. Academic Press, 662 pp.
- 425 Groh, A., H. Ewert, M. Fritsche, A. Rülke, R. Rosenau, M. Scheinert, and R. Dietrich, 2014:
426 Assessing the current evolution of the Greenland Ice Sheet by means of satellite and ground-
427 based observations. *Surveys in Geophysics*, **35**, 1459–1480, doi:10.1007/s10712-014-9287-x.

428 Hanna, E., J. Cappelen, X. Fettweis, P. Huybrechts, A. Luckman, and M. H. Ribergaard, 2009: Hy-
429 drologic response of the Greenland ice sheet: the role of oceanographic warming. *Hydrological*
430 *processes*, **23**, 7–30, doi:10.1002/hyp.7090.

431 Harden, B. E., I. A. Renfrew, and G. N. Petersen, 2011: A climatology of winterime barrier winds
432 off Southeast Greenland. *Journal of Climate*, **24**, 4701–4717, doi:10.1175/2011JCLI4113.1.

433 Heimbach, P., D. Menemenlis, M. Losch, J.-M. Campin, and C. Hill, 2010: On the formulation of
434 sea-ice models. Part 2: Lessons from multi-year adjoint sea-ice export sensitivities through the
435 Canadian Arctic Archipelago. *Ocean Modelling*, **33**, 145–158.

436 Holland, D. M., R. H. Thomas, B. de Young, M. H. Ribergaard, and B. Lyberth, 2008: Accelera-
437 tion of Jakobshavn Isbrae triggered by warm subsurface ocean waters. *Nature Geoscience*, **1**,
438 659–664.

439 Inall, M. E., T. Murray, F. R. Cottier, K. Scharrer, T. J. Boyd, K. J. Heywood, and S. L. Bevan,
440 2014: Oceanic heat delivery via Kangerdlugssuaq Fjord to the south-east Greenland ice sheet.
441 *Journal of Geophysical Research Oceans*, **119**, 631–645, doi:10.1002/2013JC009295.

442 IPCC, 2013: *Climate Change 2013: The Physical Science Basis. Contribution of Working Group I*
443 *to the Fifth Assessment Report of the Intergovernmental Panel on Climate Change*. Cambridge
444 University Press, Cambridge, United Kingdom and New York, NY, USA, 1535 pp., doi:10.
445 1017/CBO9781107415324, URL www.climatechange2013.org.

446 Jackson, R. H., F. Straneo, and D. A. Sutherland, 2014: Externally forced fluctuations in ocean
447 temperature at Greenland glaciers in non-summer months. *Nature Geoscience*, **7**, 503–508, doi:
448 10.1038/NGEO2186.

449 Khan, S. A., A. Aschwanden, A. A. Bjørk, J. Wahr, K. K. Kjeldsen, and K. H. Kjær, 2015:
450 Greenland ice sheet mass balance: a review. *Reports on Progress in Physics*, **78**, 046 801, doi:
451 10.1088/0034-4885/78/4/046801.

452 Khan, S. A., and Coauthors, 2014: Glacier dynamics at Helheim and Kangerdlugssuaq glaciers,
453 southeast Greenland, since the Little Ice Age. *The Cryosphere*, **8**, 1497–1507, doi:10.5194/
454 tc-8-1497-2014.

455 Koszalka, I. M., T. W. N. Haine, and M. G. Magaldi, 2013: Fates and travel times of Denmark
456 Strait Overflow Water in the Irminger Basin. *Journal of Physical Oceanography*, **43**, 2611–
457 2628, doi:10.1175/JPO-D-13-023.1.

458 Koszalka, I. M., M. S. Specht, T. W. N. Haine, and M. G. Magaldi, 2017: Warm water inflow
459 towards the Helheim Glacier, SE Greenland: a Lagrangian viewpoint. In preparation.

460 Large, W. G., J. C. McWilliams, and S. C. Doney, 1994: Oceanic vertical mixing: A review and
461 a model with nonlocal boundary layer parameterization. *Reviews of Geophysics*, **32**, 363–403,
462 doi:10.1029/94RG01872.

463 Leith, C. E., 1967: Diffusion approximation to inertial energy transfer in isotropic turbulence.
464 *Physics of Fluids*, **10**, 1409–1416, doi:10.1063/1.1762300.

465 Losch, M., D. Menemenlis, P. Heimbach, J.-M. Campin, and C. Hill, 2010: On the formulation
466 of sea-ice models. Part 1: Effects of different solver implementations and parameterizations.
467 *Ocean Modelling*, **33**, 129–144.

468 Luckman, A., T. Murray, R. de Lange, and E. Hanna, 2006: Rapid and synchronous ice-
469 dynamic changes in East Greenland. *Geophysical Research Letters*, **33**, L03 503, doi:10.1029/
470 2005GL025428.

471 Magaldi, M. G., T. W. N. Haine, and R. S. Pickart, 2011: On the Nature and Variability of the
472 East Greenland Spill Jet: A Case Study in Summer 2003. *Journal of Physical Oceanography*,
473 **41**, 2307–2327.

474 Marshall, J., A. Adcroft, C. Hill, L. Perelman, and C. Heisey, 1997: A finite-volume, incompress-
475 ible Navier Stokes model for studies of the ocean on parallel computers. *J. Geophys. Res.*, **102**,
476 5753–5766.

477 Menemenlis, D., and Coauthors, 2005: NASA supercomputer improves prospects for ocean cli-
478 mate research. *EOS Trans. AGU*, **86**, 89, doi:10.1029/2005EO090002.

479 Murray, T., and Coauthors, 2010: Ocean regulation hypothesis for glacier dynamics in southeast
480 Greenland and implications for ice sheet mass changes. *Journal of Geophysical Research*, **115**,
481 F03 026, doi:10.1029/2009JF001522.

482 Nguyen, A. T., D. Menemenlis, and R. Kwok, 2009: Improved modeling of the Arctic halocline
483 with a subgrid-scale brine rejection parameterization. *Journal of Geophysical Research*, **114**,
484 C11 014, doi:10.1029/2008JC005121.

485 Oltmanns, M., F. Straneo, G. W. K. Moore, and S. H. Mernild, 2014: Strong downslope wind
486 events in Ammassalik, Southeast Greenland. *Journal of Climate*, **27**, 977–993, doi:10.1175/
487 JCLI-D-13-00067.1.

488 Price, J. F., and M. O. Baringer, 1994: Outflows and deep water production by marginal seas.
489 *Progress in Oceanography*, **33**, 161200.

490 Rahmstorf, S., J. E. Box, G. Feulner, M. E. Mann, A. Robinson, S. Rutherford, and E. J. Schaffer-
491 nicht, 2015: Exceptional twentieth-century slowdown in Atlantic Ocean overturning circulation.
492 *Nature Climate Change*, **5**, 475480, doi:10.1038/NCLIMATE2554.

- 493 Rietbroek, R., S.-E. Brunnabend, J. Kusche, J. Schröter, and C. Dahle, 2016: Revisiting the
494 contemporary sea-level budget on global and regional scales. *PNAS*, **113**, 1504–1509, doi:
495 10.1073/pnas.1519132113.
- 496 Rignot, E., M. Koppes, and I. Velicogna, 2010: Rapid submarine melting of the calving faces of
497 West Greenland glaciers. *Nature Geoscience*, **3**, 187–191, doi:10.1038/NGEO765.
- 498 Rudels, B., E. Fahrbach, J. Meincke, G. Budéus, and P. Eriksson, 2002: The East Greenland
499 Current and its contribution to the Denmark Strait overflow. *Journal of Marine Science*, **59**,
500 1133–1154, doi:10.1006/jmsc.2002.1284.
- 501 Sakov, P., F. Counillon, L. Bertino, K. A. Lisæter, P. R. Oke, and A. Korabely, 2012: TOPAZ4:
502 an ocean-sea ice data assimilation system for the North Atlantic and Arctic. *Ocean Science*, **8**,
503 633–656, doi:10.5194/os-8-633-2012.
- 504 Seale, A., P. Christoffersen, R. I. Mugford, and M. O’Leary, 2011: Ocean forcing of the
505 Greenland Ice Sheet: Calving fronts and patterns of retreat identified by automatic satellite
506 monitoring of eastern outlet glaciers. *Journal of Geophysical Research*, **116**, F03013, doi:
507 10.1029/2010JF001847.
- 508 Shepherd, A., and Coauthors, 2012: A reconciled estimate of ice sheet mass balance. *Science*,
509 **338**, 1183–1189.
- 510 Straneo, F., and C. Cenedese, 2015: The dynamics of Greenland’s glacial fjords and
511 their role in climate. *Annual Reviews of Marine Science*, **7**, 89–112, doi:10.1146/
512 annurev-marine-010213-135133.
- 513 Straneo, F., and P. Heimbach, 2013: North Atlantic warming and the retreat of Greenland’s outlet
514 glaciers. *Nature*, **504**, 36–43, doi:10.1038/nature12854.

515 Straneo, F., and Coauthors, 2013: Challenges to understanding the dynamic response of Green-
516 land's marine terminating glaciers to oceanic and atmospheric forcing. *BAMS*, **94**, 1131–1144,
517 doi:10.1175/BAMS-D-12-00100.

518 Sutherland, D. A., and R. S. Pickart, 2008: The East Greenland Coastal Current: Structure, vari-
519 ability, and forcing. *Progress in Oceanography*, **78**, 58–77.

520 Sutherland, D. A., F. Straneo, and R. S. Pickart, 2014: Characteristics and dynamics of two major
521 Greenland glacial fjords. *Journal of Geophysical Research*, **119**, doi:10.1002/2013JC009786.

522 Sutherland, D. A., F. Straneo, G. B. Stenson, F. J. M. Davidson, M. O. Hammill, and A. Rosing-
523 Asvid, 2013: Atlantic water variability on the SE Greenland continental shelf and its re-
524 lationship to SST and bathymetry. *Journal of Geophysical Research*, **118**, 847–855, doi:
525 10.1029/2012JC008354.

526 Thomas, R., E. Frederick, W. Krabill, S. Manizade, and C. Martin, 2009: Recent changes on
527 Greenland outlet glaciers. *Journal of Glaciology*, **55**, 147–162.

528 van den Broeke, M., and Coauthors, 2009: Partitioning recent Greenland mass loss. *Science*, **326**,
529 984–986, doi:10.1126/science.1178176.

530 Velicogna, I., and J. Wahr, 2013: Time-variable gravity observations of ice sheet mass balance:
531 Precision and limitations of the GRACE satellite data. *Geophysical Research Letters*, **40**, 3055–
532 3063, doi:10.1002/grl.50527.

533 von Appen, W.-J., and Coauthors, 2014: The East Greenland Spill Jet as an important component
534 of the Atlantic Meridional Overturning Circulation. *Deep-Sea Research I*, **92**, 75–84, doi:10.
535 1016/j.dsr.2014.06.002.

536 **LIST OF FIGURES**

537 **Fig. 1.** (a) Model domain for the simulations. Depth contours have been drawn at 3000, 2000, 1000,
538 500, 400 and 0 m depth. The shelf region shallower than 400 m depth is shaded light gray;
539 dark gray is land. The blue and red dashed lines are the transects used in section 3, the cyan
540 line is where the particles are released, and the magenta line in the fjord mouth is the KS'
541 CTD section used for model validation in Section 2b. The colored arrows roughly indicate
542 the pathways of the main currents. EGC = East Greenland Current; IC = Irminger Current;
543 DWBC = Deep Western Boundary Current; KO = Kögur section; FF = Faxaflói section.
544 KF = Kangerdlugssuaq Fjord, SF = Sermilik Fjord. (b) Close up of the Kangerdlugssuaq
545 Glacier-Fjord-Trough area. Shading and depth contours are the same as in panel (a), with
546 the 200m and 300m isobaths added to bring out bathymetric features on the shelf. KS =
547 Kangerdlugssuaq Section; KS' = CTD line used for validation; KG = Kangerdlugssuaq
548 Glacier; KF = Kangerdlugssuaq Fjord; KT = Kangerdlugssuaq Trough; ØB = Øst Bank; DB
549 = Dohrn Bank. 28

550 **Fig. 2.** Temperature (°C, left column) and salinity (psu, right column) along the Faxaflói section
551 (FF, red dashed line in Figure 1). (a/b) Composite of high-resolution CTD observations;
552 (c/d) model annual-mean hydrography; (e/f) model-mean over July-November period; (g/h)
553 model-mean over January-May period. 29

554 **Fig. 3.** As Figure 2, but for the Kögur section (KO, blue dashed line in Figure 1). 30

555 **Fig. 4.** (top) Potential temperature (°C), (middle) salinity (psu), and (bottom) potential density (kg
556 m⁻³) along the KS' section (magenta line in Figure 1). Observations were taken on 28
557 September 2007. Model fields are an average over the 5 days before to 5 days after this date.
558 The colored dashed contours in the bottom panels indicate water masses: warm Polar Sur-
559 face Water (black), Polar Surface Water (cyan), modified Atlantic Water (red), and Denmark
560 Strait Overflow Water (green). 31

561 **Fig. 5.** Seasonal-mean sections at the particle release section (cyan line in Figure 1) for potential
562 temperature (°C, top) and salinity (bottom). JASON = July-November; JFMAM = January-
563 May. 32

564 **Fig. 6.** Particles trajectories per season. The shading indicates the fraction of particle trajectories per
565 control section reaching that location in the model domain. Only values exceeding 1 % are
566 shaded. Color coding is the same as in Figure 1. The 400-m isobath is shown as the dashed
567 gray contour. The black solid contour represents the offshore edge of the area exceeding 50
568 % sea-ice coverage. Note that the pathways are 3-dimensional, but are projected onto the
569 horizontal plane in this figure. 33

570 **Fig. 7.** Transit time distributions in summer (left) and winter (right). Color coding is the same as in
571 Figure 1. 34

572 **Fig. 8.** The fraction of particles from each upstream control section of the total number of parti-
573 cles in the season as a function of origin section and the depth that they were released at
574 Kangerdlugssuaq section (solid lines). The total number of particles per season (N) is noted
575 in each panel. The colored percentages indicate the fractionation of this total over the two
576 origin sections for that season; the bracketed numbers give the percentage of the total num-
577 ber of particles released, for completeness. The dashed lines are the required fractionations
578 to obtain the water properties at Kangerdlugssuaq section by mixing of FF and KO water
579 masses. The black dotted line is the zero-fraction grid line. 35

580 **Fig. 9.** (a/b) Temperature-salinity diagrams for JASON (left) and JFMAM (right) particle trajectories. The dots are the θ/S characteristics at the control sections. Red dots indicate properties
581 at Faxaflói, magenta dots the θ/S values of these same particles at Kangerlugssuaq Section,
582 blue dots represent the θ/S properties at Kögur, and green their transformed values at
583 Kangerlugssuaq Section. The squares are the mean values over all particles in that subset.
584 (c/d) Comparison between mixing model results (Eq. 1) using seasonally varying values
585 (black squares), annual mean θ/S properties at the upstream control sections (cyan asterisks),
586 and annual mean volume fractions (magenta asterisks). 36
587

588 **Fig. 10.** Comparison of regions where FF particles lose heat at a rate exceeding $0.02\text{ }^\circ\text{C}$ per day (red
589 shading) and where KO particles gain heat exceeding the same rate (blue shading). 37

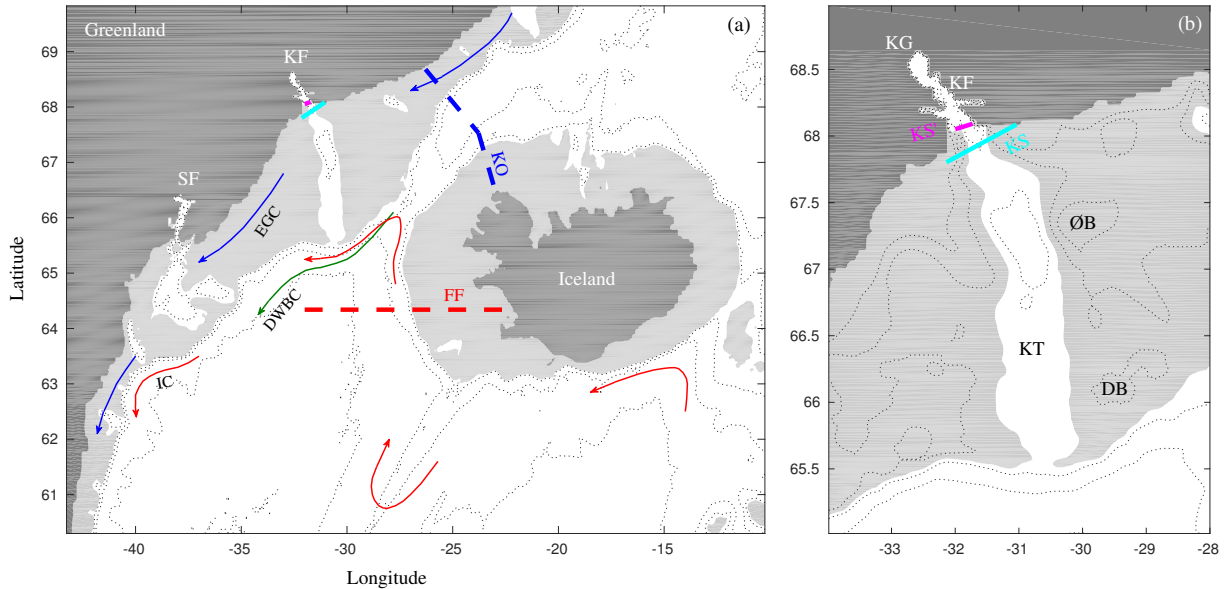


FIG. 1: (a) Model domain for the simulations. Depth contours have been drawn at 3000, 2000, 1000, 500, 400 and 0 m depth. The shelf region shallower than 400 m depth is shaded light gray; dark gray is land. The blue and red dashed lines are the transects used in section 3, the cyan line is where the particles are released, and the magenta line in the fjord mouth is the KS' CTD section used for model validation in Section 2b. The colored arrows roughly indicate the pathways of the main currents. EGC = East Greenland Current; IC = Irminger Current; DWBC = Deep Western Boundary Current; KO = Kögur section; FF = Faxaflói section. KF = Kangerdlugssuaq Fjord, SF = Sermilik Fjord. (b) Close up of the Kangerdlugssuaq Glacier-Fjord-Trough area. Shading and depth contours are the same as in panel (a), with the 200m and 300m isobaths added to bring out bathymetric features on the shelf. KS = Kangerdlugssuaq Section; KS' = CTD line used for validation; KG = Kangerdlugssuaq Glacier; KF = Kangerdlugssuaq Fjord; KT = Kangerdlugssuaq Trough; ØB = Øst Bank; DB = Dohrn Bank.

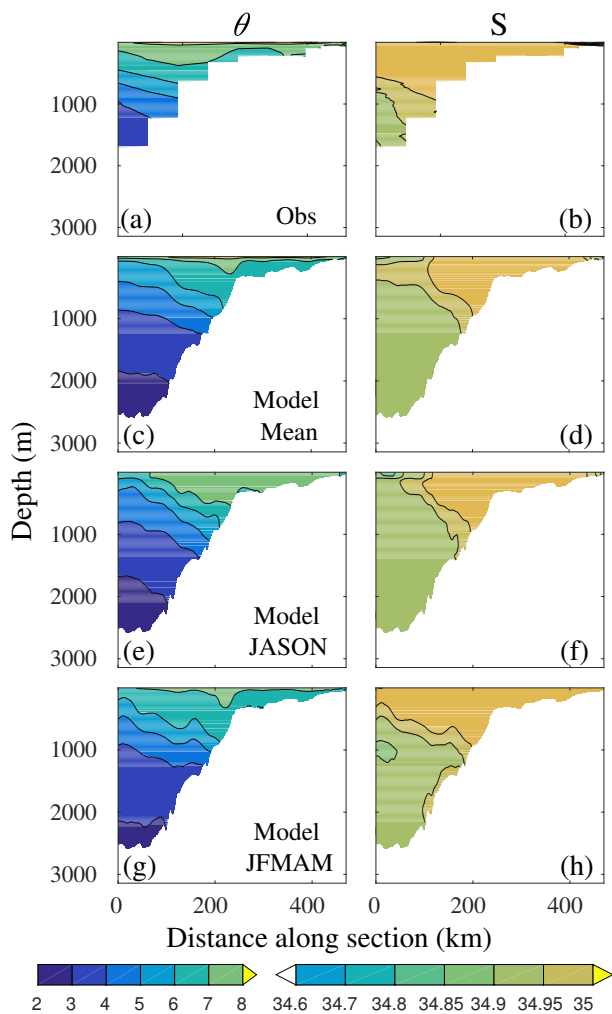


FIG. 2: Temperature ($^{\circ}\text{C}$, left column) and salinity (psu, right column) along the Faxaflói section (FF, red dashed line in Figure 1). (a/b) Composite of high-resolution CTD observations; (c/d) model annual-mean hydrography; (e/f) model-mean over July-November period; (g/h) model-mean over January-May period.

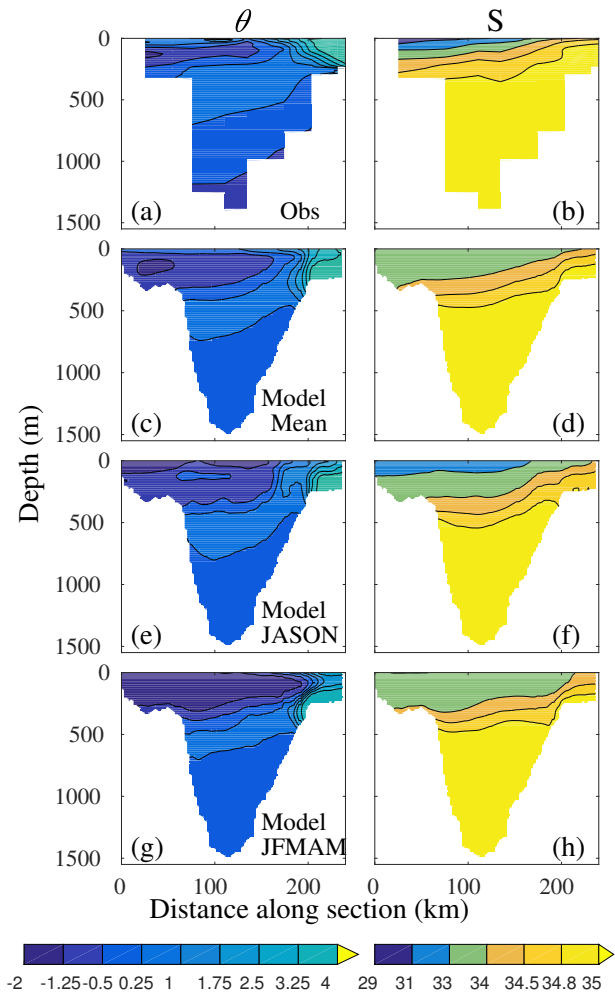


FIG. 3: As Figure 2, but for the Kögür section (KO, blue dashed line in Figure 1).

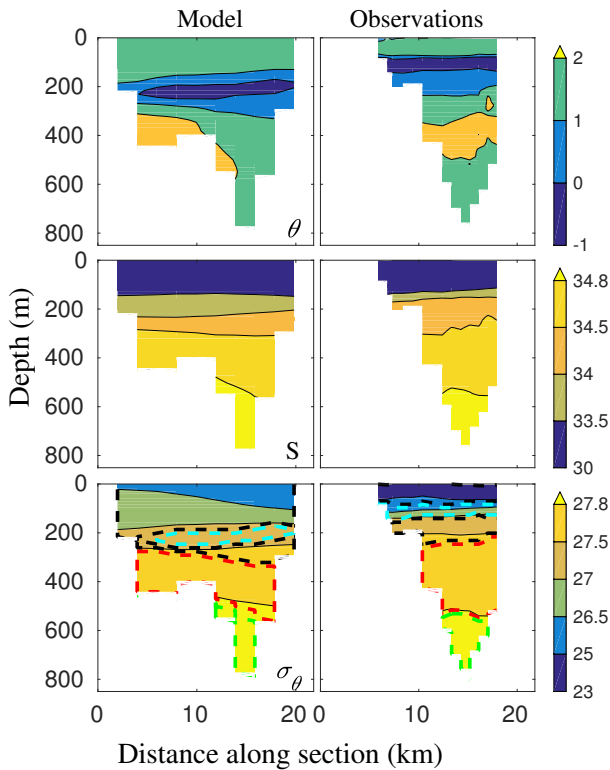


FIG. 4: (top) Potential temperature ($^{\circ}\text{C}$), (middle) salinity (psu), and (bottom) potential density (kg m^{-3}) along the KS' section (magenta line in Figure 1). Observations were taken on 28 September 2007. Model fields are an average over the 5 days before to 5 days after this date. The colored dashed contours in the bottom panels indicate water masses: warm Polar Surface Water (black), Polar Surface Water (cyan), modified Atlantic Water (red), and Denmark Strait Overflow Water (green).

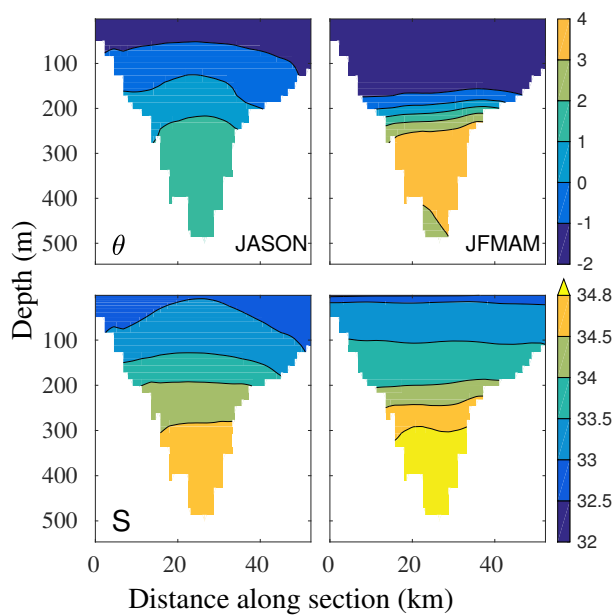


FIG. 5: Seasonal-mean sections at the particle release section (cyan line in Figure 1) for potential temperature ($^{\circ}\text{C}$, top) and salinity (bottom). JASON = July-November; JFMAM = January-May.

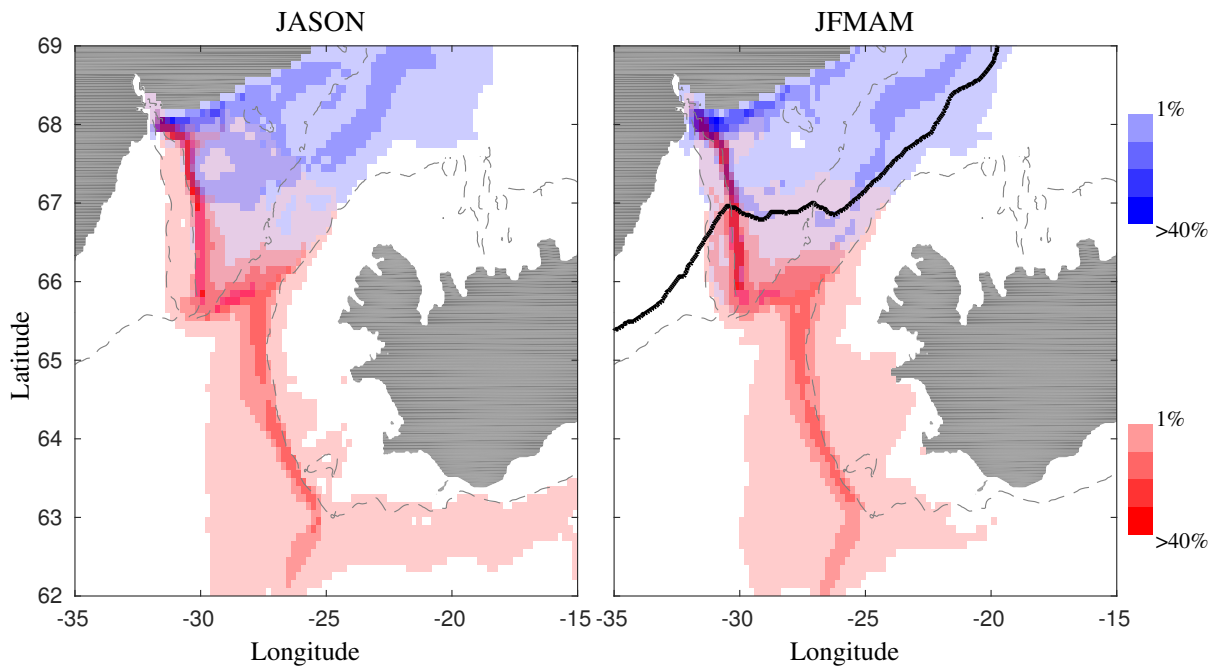


FIG. 6: Particles trajectories per season. The shading indicates the fraction of particle trajectories per control section reaching that location in the model domain. Only values exceeding 1 % are shaded. Color coding is the same as in Figure 1. The 400-m isobath is shown as the dashed gray contour. The black solid contour represents the offshore edge of the area exceeding 50 % sea-ice coverage. Note that the pathways are 3-dimensional, but are projected onto the horizontal plane in this figure.

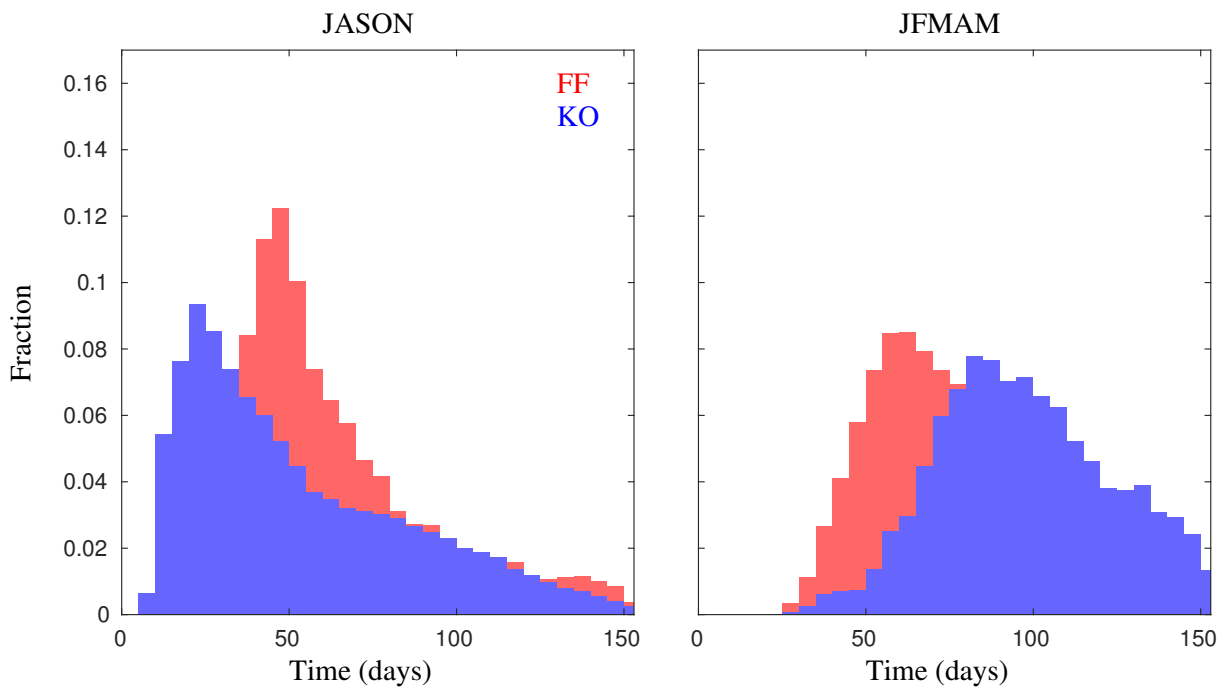


FIG. 7: Transit time distributions in summer (left) and winter (right). Color coding is the same as in Figure 1.

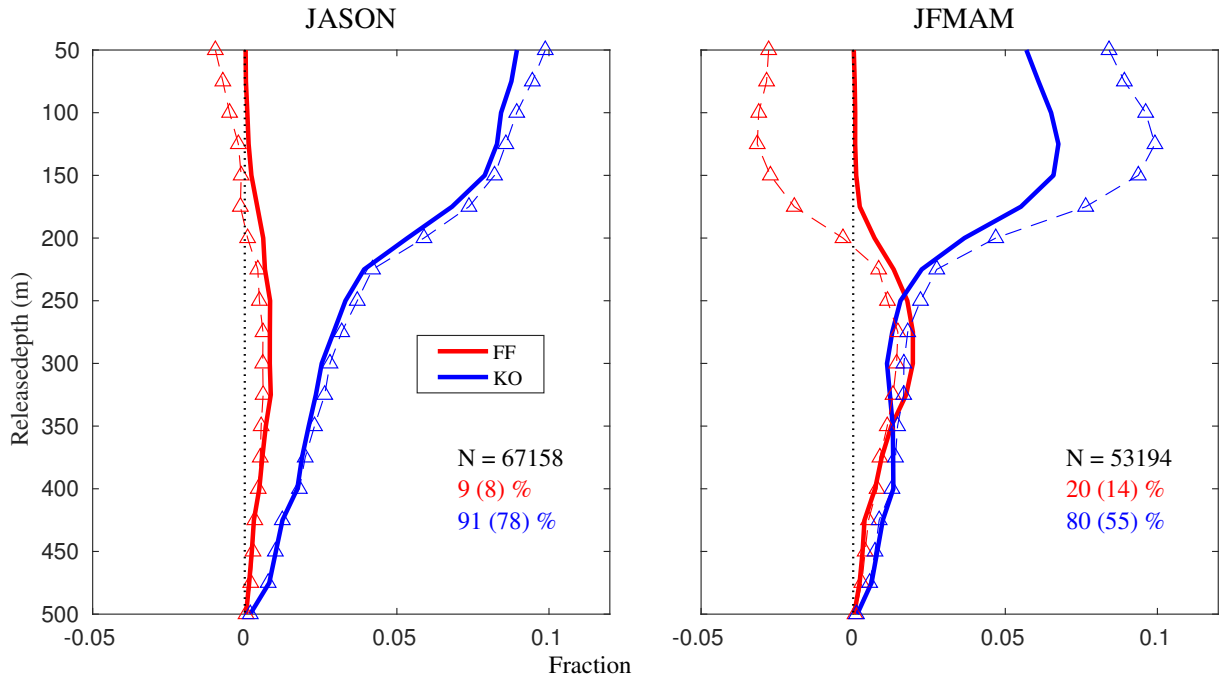


FIG. 8: The fraction of particles from each upstream control section of the total number of particles in the season as a function of origin section and the depth that they were released at Kangerdlugssuaq section (solid lines). The total number of particles per season (N) is noted in each panel. The colored percentages indicate the fractionation of this total over the two origin sections for that season; the bracketed numbers give the percentage of the total number of particles released, for completeness. The dashed lines are the required fractionations to obtain the water properties at Kangerdlugssuaq section by mixing of FF and KO water masses. The black dotted line is the zero-fraction grid line.

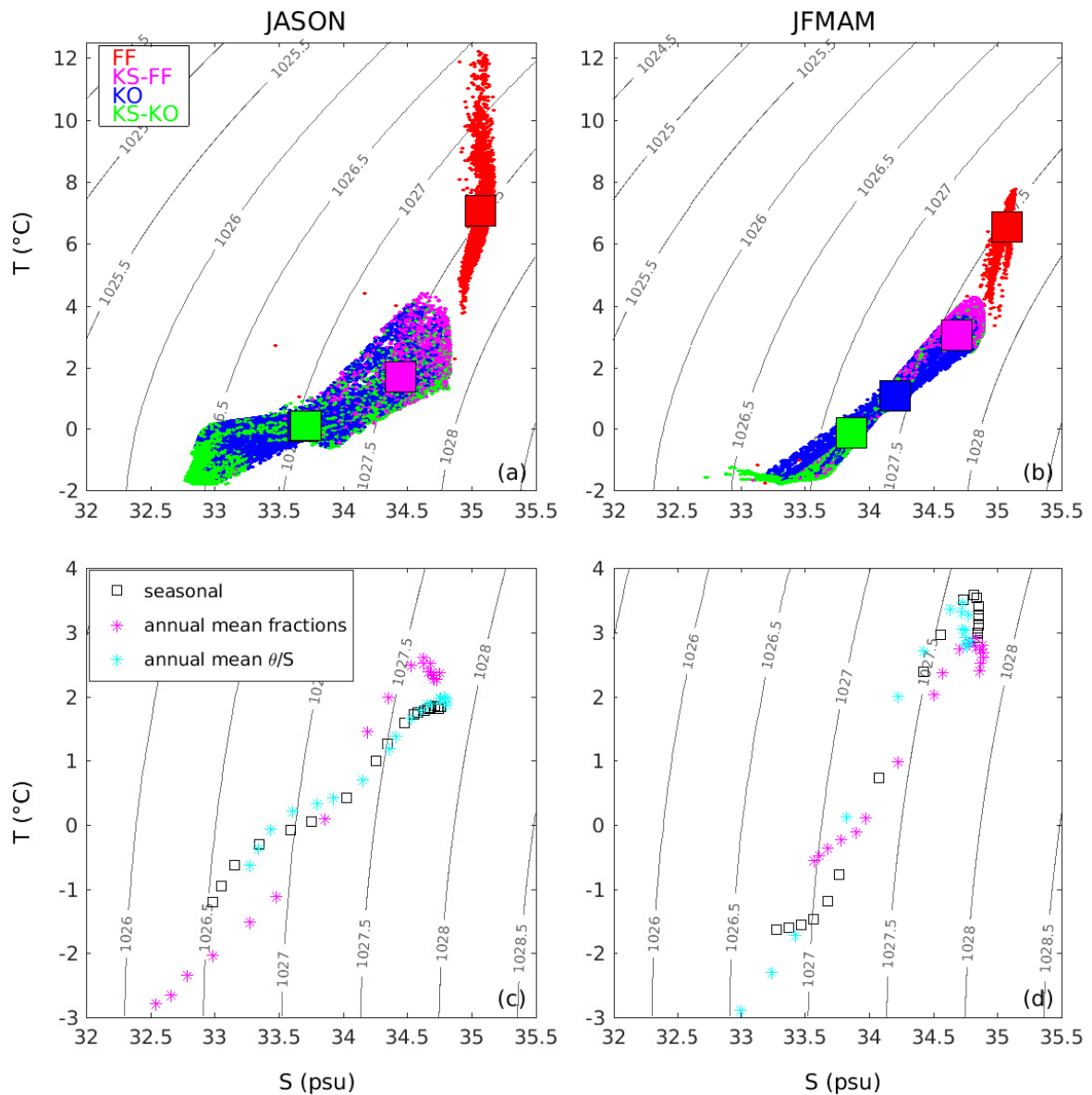


FIG. 9: (a/b) Temperature-salinity diagrams for JASON (left) and JFMAM (right) particle trajectories. The dots are the θ/S characteristics at the control sections. Red dots indicate properties at Faxaflói, magenta dots the θ/S values of these same particles at Kangerlugssuaq Section, blue dots represent the θ/S properties at Kögur, and green their transformed values at Kangerlugssuaq Section. The squares are the mean values over all particles in that subset. (c/d) Comparison between mixing model results (Eq. 1) using seasonally varying values (black squares), annual mean θ/S properties at the upstream control sections (cyan asterisks), and annual mean volume fractions (magenta asterisks).

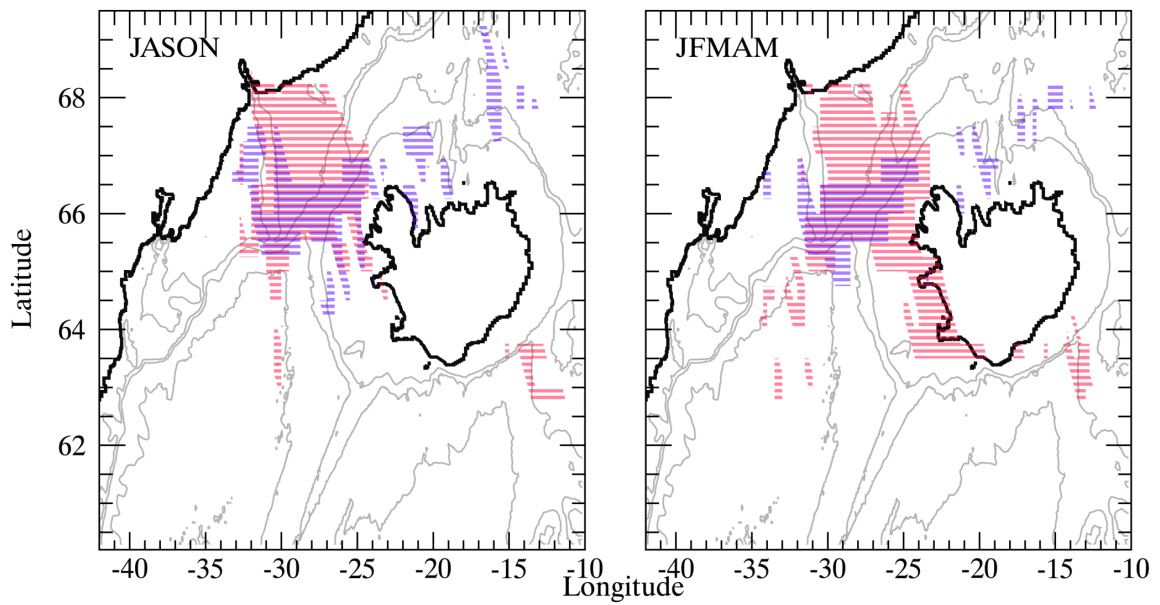


FIG. 10: Comparison of regions where FF particles lose heat at a rate exceeding $0.02 \text{ }^\circ\text{C}$ per day (red shading) and where KO particles gain heat exceeding the same rate (blue shading).